

MODELING CORONAL RESPONSE IN DECAYING ACTIVE REGIONS WITH MAGNETIC FLUX TRANSPORT AND STEADY HEATING

IGNACIO UGARTE-URRA,¹ HARRY P. WARREN,¹ LISA A. UPTON,² AND PETER R. YOUNG^{3,4,5}

¹*Space Science Division, Naval Research Laboratory, Washington, DC 20375, USA*

²*High Altitude Observatory, National Center for Atmospheric Research, 3080 Center Green Dr., Boulder, CO 80301, USA*

³*College of Science, George Mason University, 4400 University Drive, Fairfax, VA 22030, USA*

⁴*NASA Goddard Space Flight Center, Code 671, Greenbelt, MD 20771, USA*

⁵*Northumbria University, Newcastle Upon Tyne NE1 8ST, UK*

ABSTRACT

We present new measurements of the dependence of the Extreme Ultraviolet radiance on the total magnetic flux in active regions as obtained from the Atmospheric Imaging Assembly (AIA) and the Helioseismic and Magnetic Imager on board the Solar Dynamics Observatory (SDO). Using observations of nine active regions tracked along different stages of evolution, we extend the known radiance - magnetic flux power-law relationship ($I \propto \Phi^\alpha$) to the AIA 335 Å passband, and the Fe XVIII 93.93 Å spectral line in the 94 Å passband. We find that the total unsigned magnetic flux divided by the polarity separation (Φ/D) is a better indicator of radiance for the Fe XVIII line with a slope of $\alpha = 3.22 \pm 0.03$. We then use these results to test our current understanding of magnetic flux evolution and coronal heating. We use magnetograms from the simulated decay of these active regions produced by the Advective Flux Transport (AFT) model as boundary conditions for potential extrapolations of the magnetic field in the corona. We then model the hydrodynamics of each individual field line with the Enthalpy-based Thermal Evolution of Loops (EBTEL) model with steady heating scaled as the ratio of the average field strength and the length (\bar{B}/L) and render the Fe XVIII and 335 Å emission. We find that steady heating is able to partially reproduce the magnitudes and slopes of the EUV radiance - magnetic flux relationships and discuss how impulsive heating can help reconcile the discrepancies. This study demonstrates that combined models of magnetic flux transport, magnetic topology and heating can yield realistic estimates for the decay of active region radiances with time.

Keywords: Sun: corona — Sun: magnetic fields

1. INTRODUCTION

The emergence of strong magnetic fields on the solar surface gives rise to active regions, areas of large radiative output in the X-rays and the Extreme Ultraviolet (EUV) solar spectrum. Their radiance is extremely well correlated with the total (unsigned) magnetic flux contained in those fields (see e.g. Gurman et al. 1974; Schrijver 1987; Fisher et al. 1998; Benevolenskaya et al. 2002; Fludra et al. 2002; Pevtsov et al. 2003; van Driel-Gesztelyi et al. 2003; Fludra & Ireland 2008; Ugarte-Urra et al. 2015), but the nature of the coupling between the magnetic field changes and the modulation of the plasma response in the atmosphere remains to be understood.

Active regions exhibit radiative changes at a large range of spatial and temporal scales. As the emission of the plasma in the corona is fundamentally dependent on its hydrodynamic state (density and temperature), a significant part of the studies have gone into identifying, characterizing and modeling the fundamental structures of the atmosphere: coronal loops. Recent reviews (Klimchuk 2006; Reale 2014) summarize the progress made in this area by high resolution imaging, spectroscopy and hydrodynamic modeling, mostly in 1D. Latest efforts include the development of magnetohydrodynamic models of magnetic flux tubes in 3D with thermal conduction and radiation (Dahlburg et al. 2016; Reale et al. 2016) that allow for forward modeling of intensities and direct comparisons with observations.

Studying loops in isolation can be challenging particularly when tracking their evolution in temperature and across different spectral bands. There is always potential contamination from other loops along the same line of sight, especially at ~ 2 MK. Many studies have therefore opted to model the complete active region, or even the full Sun, at any given instant as a set of loops and then compare the integrated emission to remote sensing images (Schrijver et al. 2004; Warren & Winebarger 2006, 2007; Winebarger et al. 2008; Lundquist et al. 2008a,b; Dudík et al. 2011). These sets of models use 0D or 1D hydrodynamics solutions for each individual loop in the simulated domain and an ad hoc heating. With the improvement in performance of high-end computing, these comparisons are now being done against 3D magnetohydrodynamical (MHD) radiative models, with rigid topology and parametrized heating (Mok et al. 2005, 2016) or forcing at the lower boundary that advects the field and generates the atmospheric heating through ohmic dissipation (Peter et al. 2004; Gudiksen & Nordlund 2005; Peter et al. 2006; Zacharias et al. 2009; Hansteen et al. 2010; Bingert & Peter 2011; Martínez-Sykora et al. 2011; Zacharias et al. 2011; Testa et al. 2012; Bourdin et al. 2013; Olluri et al. 2015).

These two approaches investigate the heating and atmospheric response on short timescales, minutes to hours, but

there is an equally relevant component of active region heating at longer time scales. Active region lifetimes span days to weeks with both total magnetic flux and radiance going through changes of several orders of magnitude (see review on active region evolution by van Driel-Gesztelyi & Green 2015). After the emergence of an active region, where the region grows in size, magnetic flux and polarity separation, magnetic fields on the surface are transported by surface flows, namely differential rotation, meridional circulation and convection. These processes cause the magnetic elements to spread over increasing areas and cancel with nearby magnetic elements. In this diffusive evolution part of the observed flux is lost in the noise. The overall result is, first a rapid increase of the total observed magnetic flux, followed by a slower decay after the peak, that is accompanied by a similar increase and then drop in the radiative output (e.g. Ugarte-Urra & Warren 2012). We showed in Ugarte-Urra et al. (2015) (hereafter Paper I) that a state-of-the-art magnetic flux transport model such as the Advective Flux Transport (AFT) (Upton & Hathaway 2014b,a) model can make realistic predictions of the total magnetic flux decline in an active region. Different coronal heating theories predict different scalings for how the change in the magnetic field can affect the atmosphere (e.g. Mandrini et al. 2000). One scaling that has been most successful to reproduce observables in the corona is heating that depends on the field strength and length of coronal loops (e.g. Warren & Winebarger 2006, 2007; Lundquist et al. 2008b), two quantities that change over the evolutionary time scales of active regions.

In the present paper, we investigate whether we can make use of this improved understanding of magnetic flux transport to model the coronal response over long periods of time. We use the AFT simulated magnetic field evolution of nine active regions as a boundary condition for a quasi-static steady heating model, a steady heating scenario that has proven to be successful to model the high temperature plasma in active region snapshots. We show that we can indeed predict the decline of EUV emission as a function of time and magnetic flux, and we discuss potential improvements when incorporating more sophisticated models. Furthermore, we find that the observed Fe XVIII emission is better described by the combination of the magnetic flux and the mean loop length than by the magnetic flux alone. This provided further evidence for a coronal heating rate that is parameterized by magnetic flux and loop length.

2. OBSERVATIONS

We looked at a set of nine active regions previously selected for a study of their long-term evolution in the context of magnetic flux transport and decay (see Paper I). The regions, from the period January 2011 – July 2013, were cho-

sen for their isolation, i.e. regions minimally impacted by neighboring active regions. In that investigation we used integrated 304 Å light curves as a proxy for active region development (emergence, growth and decay) and found that it can also be used as a proxy for total unsigned magnetic flux. Several regions were observed from emergence (11158,11672,11726,11765) while others are seen in evolved stages. The 304 Å evolution lightcurves can be consulted in Figure 3 of [Paper I](#).

In the current study, we turn our focus to the response of those regions in the corona. We inspected EUV coronal images from the Atmospheric Imaging Assembly (AIA) ([Lemen et al. 2012](#)) on board the *Solar Dynamics Observatory* ([Pesnell et al. 2012](#)). AIA takes high cadence (12 s) and high-resolution (0.6'' per pixel) images of the Sun in ten narrow-band filters. For our study, active regions were tracked from limb to limb at a cadence of 1 hr, sufficient to characterize the gradual evolution. The 94 Å band is centered at the spectral line Fe XVIII 93.93 Å, with a formation temperature of 7×10^6 K. This line dominates the emission in active region and flare conditions ([O'Dwyer et al. 2010](#); [Testa & Reale 2012](#); [Teriaca et al. 2012](#)), but contributions from Fe VIII, Fe X and Fe XIV ions can be important in the quiet Sun. As shown by [Warren et al. \(2012\)](#) and [Teriaca et al. \(2012\)](#), the “hot” Fe XVIII line emission in the channel can be isolated by removing the contaminating “warm” component from a weighted combination of emission from the 193 Å and the 171 Å channels. In [Ugarte-Urra & Warren \(2014\)](#) we used this method to study the temporal evolution of individual coronal loops in Fe XVIII emission. In that study we argued that the Fe XVIII line is a good diagnostic for the study of loops in active region cores because the temperature response contains the peak of their emission measure distribution ($\sim 4 \times 10^6$ K) and it is narrower than X-ray broad-band filters observing in those temperature ranges. In the present paper, we are interested in the global properties of the active region and we integrate the Fe XVIII counts to derive the total radiative output in that line. We also use images in the 335 Å band, dominated by Fe XVI with a formation temperature of 2.8×10^6 K. The latter is a more traditional temperature range for the study of loops and active regions and facilitates the comparison to other results. We applied a time dependent sensitivity correction for 335 Å images that is available in the standard software distribution (`aia_get_response.pro`). In the rest of the paper we refer to counts per second in the 335 channel, and this always means the counts per second corrected to be as if the images were obtained at the start of the mission rather than the actual measured counts. In contrast to the 94 Å passband, we do not have an empirical method to isolate the Fe XVI from other cooler contributions ([O'Dwyer et al.](#)

[2010](#)) and we perform the analysis over the whole filter spectrally integrated signal.

We computed the total unsigned magnetic flux for every active region as a function of time: $\Phi(t) = \int |B_z(t)| dA$ where A is area on the surface and B_z is the vertical magnetic field. We used line-of-sight magnetograms from the Helioseismic and Magnetic Imager/SDO ([Scherrer et al. 2012](#); [Schou et al. 2012](#)), correcting for line of sight projection angle effects for both the pixel areas and the observed flux densities.

3. MAGNETIC FLUX AND EUV RADIANCE

It is well known that the EUV and X-ray response of the solar corona scales up with the magnetic flux content. This is normally presented in the form of a magnetic flux-luminosity relationship that has been explored for a variety of solar phenomena such as active regions, coronal bright points, quiet Sun and even other stars ([Pevtsov et al. 2003](#)). In the case of active regions, these scatter plot relationships have been generally constructed statistically, where different magnetic fluxes and luminosities (or radiances) are provided by active regions of different size and strength ([Gurman et al. 1974](#); [Schrijver 1987](#); [Fisher et al. 1998](#); [Fludra et al. 2002](#); [Fludra & Ireland 2008](#)). There are also examples of scatter plots made out of the evolving properties of a single region (e.g. [van Driel-Gesztelyi et al. 2003](#)) or a coronal bright point ([Ugarte-Urra 2004](#)). In this study, we combine both approaches. We first track the total unsigned flux and EUV radiance changes in single active regions from birth to decay. Then we combine the results for multiple cases, the nine active regions in our dataset. In [Paper I](#) we did exactly that for the 304 Å intensities. Here we extend it to the 335 Å channel and the Fe XVIII component in the 94 Å channel.

Figure 1 shows the scatter plot of the total number of AIA Fe XVIII and 335 Å counts per second as a function of total unsigned magnetic flux for each active region in the dataset. Each datapoint corresponds to a particular instant in the evolution of the region while it transits within 60° of Sun center. In the case of NOAA 11158, 11193 and 11726, the longest lived regions in the dataset (see Figure 1 in [Paper I](#)), we include data points for two rotations. Counts were integrated within a rectangular field-of-view with sides ranging from 100'' to 325'' depending on the size of the active region and above a threshold of 2 and 4 DN s⁻¹ for Fe XVIII and 335 Å images respectively. Following [Fludra & Ireland \(2008\)](#) we only considered magnetic flux densities in the range 90 – 900 G, within the same rectangular field-of-views. The 900 G is a conservative limit to exclude sunspots. Preliminary calculations with a lower threshold of 20 G and including sunspot flux, as used for 304 Å in [Paper I](#), resulted in similar overall results with minor changes ($\lesssim 0.1$) in the slopes.

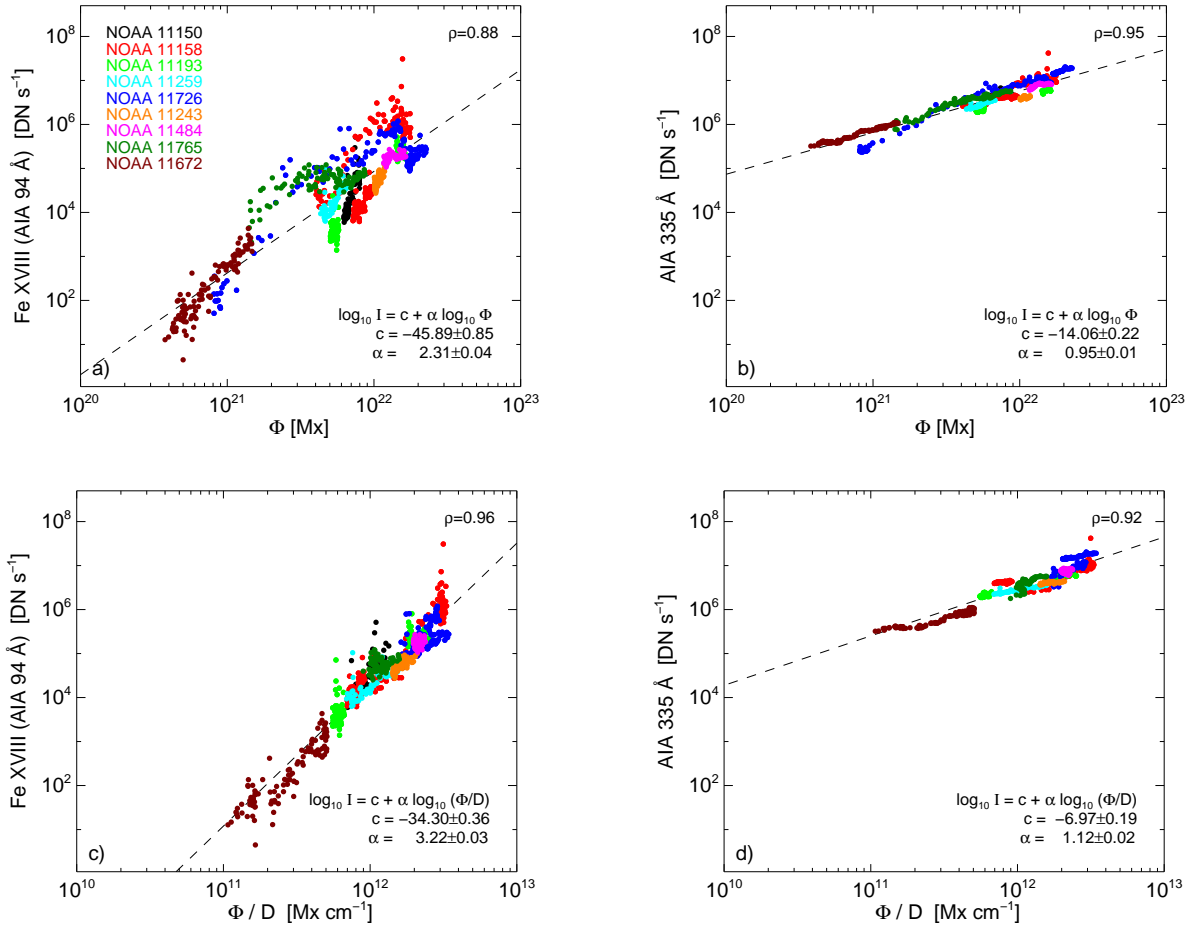


Figure 1. Scatterplot of the EUV radiance and total unsigned magnetic flux for nine active regions. The different points in each region correspond to different times in the evolution. Panels c) and d) show the total unsigned magnetic flux divided by the separation between the centroid of the two polarities. Dashed lines are linear fits to the logarithmic quantities. ρ is the Pearson correlation coefficient.

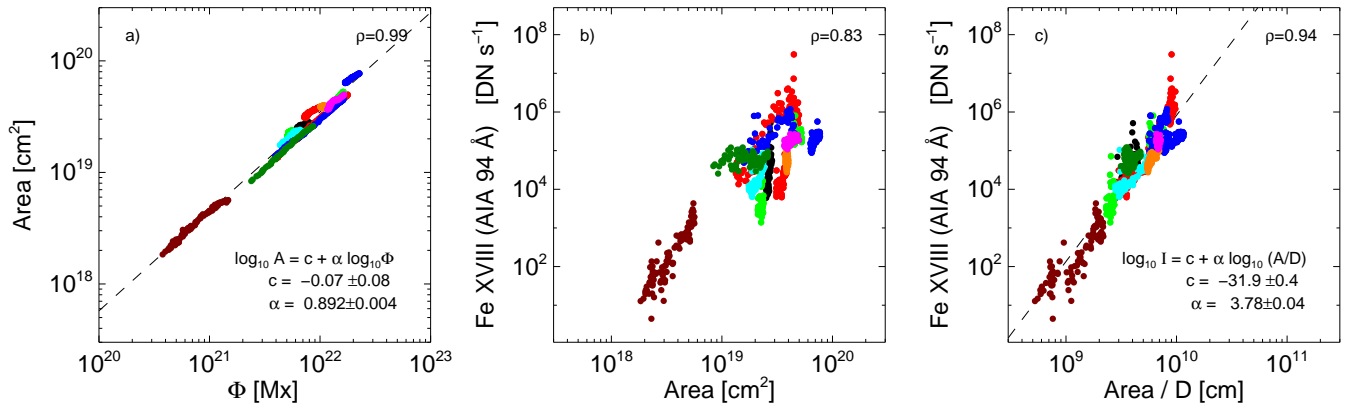


Figure 2. Scatterplot of the a) active region magnetic area versus total unsigned magnetic flux, b) Fe XVIII radiance versus magnetic area, and c) Fe XVIII radiance versus the ratio of magnetic area to polarity separation. Dashed lines are linear fits. ρ is the Pearson correlation coefficient. Colors represent different active regions, same as Figure 1.

The log-log plots show that, as expected, the correlation between the two quantities for both channels is high and is well represented by a power law fit ($I \propto \Phi^\alpha$). The slope in 335 Å is $\alpha = 0.95$ close to the 1.1 – 1.3 values obtained for Fe XVI from CDS spectroscopic measurements (Fludra et al. 2002; Fludra & Ireland 2008), although it is hard to make direct comparisons between these studies when different units are used as Fludra & Ireland (2008) rightly pointed out. The slope for Fe XVIII is much steeper (2.31), which is a consistent trend with previous estimates (1.6 – 2) of hotter plasma using X-ray broad band filters (e.g. Warren & Winebarger 2006; van Driel-Gesztelyi et al. 2003; Benevolenskaya et al. 2002), but Fisher et al. (1998) reported 1.19 in luminosity units. The dispersion for the Fe XVIII slope is larger than 335 with trends for the individual regions that seem to diverge at times from the overall power law fit. Flaring activity has not been filtered out in the analysis and could contribute to the dispersion, but most regions only produced C-class flares and only NOAA 11158 produced X and M-class flares, visible as the extreme values in Fe XVIII counts in Figure 1a.

Previous studies already conclude that the area of the active region, highly correlated to the total magnetic flux (Figure 2a), is the dominant factor in the flux relationship to the radiance (Schrijver 1987; Fisher et al. 1998; Fludra & Ireland 2008). This is evident when we see the similitude between the Fe XVIII radiance dependence with the total magnetic area (Figure 2b) and the flux dependence in Figure 1a.

In terms of the coupling between magnetic flux and radiance, several studies identify the ratio of the loop’s average field strength to its length (\bar{B}/L) as a volumetric heating scaling that has been successful to model high temperature radiation in active regions (Warren & Winebarger 2006, 2007; Lundquist et al. 2008b). If the heating of loops depends on \bar{B} and L , it seems natural to consider how important for the radiance is the spread of the corresponding total magnetic flux and area. A similar argument was made by Fludra & Ireland (2003) who tested it with CDS Fe XVI data and found a very weak dependence on an average loop length.

In the Figures 1c and 1d we show how the relationship changes when we add a characteristic length D to our dataset. We have chosen D as the separation between the magnetic flux density weighted centroids of the two polarities (within 90 – 900 G), calculated as the great-circle distance

$$D = R_\odot \arccos(\cos \theta_1 \cos \theta_2 \cos(\phi_1 - \phi_2) + \sin \theta_1 \sin \theta_2)$$

where θ and ϕ are the latitude and longitude of the centroids and R_\odot the solar radius. These scatter plots have fewer points per active region because we had to visually filter out instances in the evolution, e.g. emergence, when the automatic distance measurements failed. It is worth noting that despite the already high correlation between the Fe XVIII counts and the magnetic flux, adding the characteristic length

does improve the correlation and the power-law fit, and increases the slope to 3.22 suggesting that the total flux per characteristic separation length is a better indicator for hot lines such as Fe XVIII. This is also true for the area (Figure 2c) meaning that in terms of intensity it is relevant how spread that area is, not surprising if the heating is inversely proportional to the loop length. Until now, however, this dependence on length has remained undetected. One possible explanation is the spectral line selection. We have argued that Fe XVIII is a particularly good diagnostic in active regions for its formation temperature and its spectral purity. Most studies use cooler EUV lines (e.g. Fe XVI), or X-ray broad band filters that integrate signal from those lower temperatures. Indeed, the influence of the separation for 335 Å is minimal (even producing a slightly worse fit), which is consistent with previous results such as Fludra & Ireland (2003) that report a weak dependence for Fe XVI. In this line, the filling of the active region coronal volume with signal is larger than that of Fe XVIII, with more loops at different lengths contributing to the integrated intensity. In a later discussion we also show that Fe XVIII and Fe XVI lines can be diagnostics for different phases in the evolution of a coronal loop.

In the following section we use global active region modeling to see whether these measurements are consistent with our current understanding of heating in active regions.

4. MODELING

The flux-radiance relationships tell us that by knowing the total magnetic flux of an active region, we are able to estimate the radiance of that region in X-rays and the EUV. In Paper I we argued that a state-of-the-art magnetic flux transport model such as the Advective Flux Transport (AFT) (Upton & Hathaway 2014b,a) model is already capable of making realistic predictions of the total magnetic flux decay in an active region. Therefore relationships such as those in Figures 1 combined with the AFT model flux predictions, in principle, allow us to make reasonable estimates of AIA Fe XVIII and 335 Å counts.

In the following sections, we go beyond the empirical description and investigate whether the model of the flux decay combined with a simple coronal heating model can reproduce these observed relationships. The actual coronal heating mechanism is still not known and while there are some 3D MHD efforts to study the problem from first principles, simulations are still constrained to brief periods of time of individual loops or small active regions. As we are looking at a set of nine active regions evolving over periods of weeks and months, our approach is simpler. We look at snapshots of the active region magnetic evolution determined by the AFT model and we model the 3D magnetic topology with a potential magnetic field extrapolation. The coronal response of

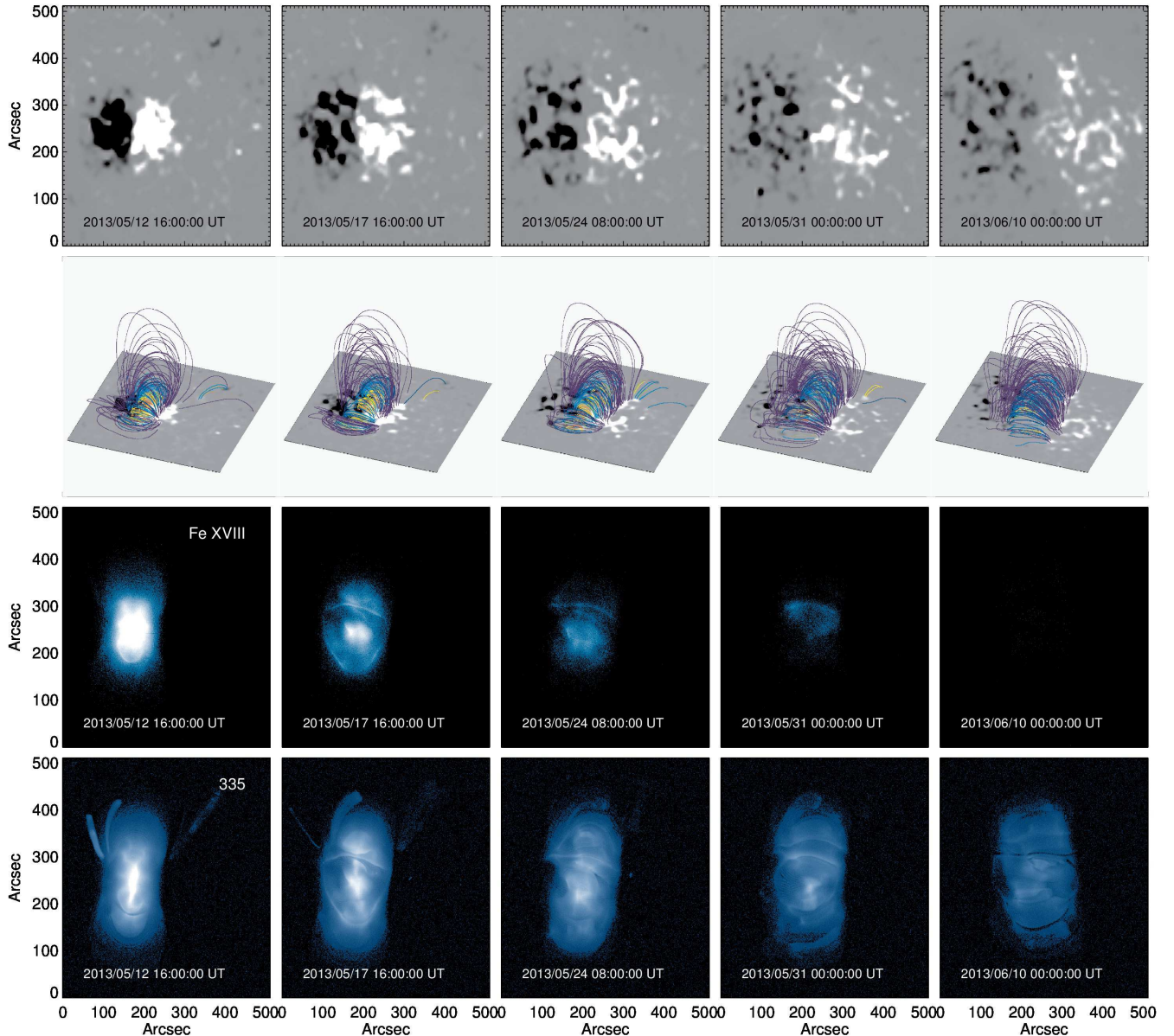


Figure 3. Representative simulation of active region decay that combines three models: magnetic flux transport, magnetic topology and hydrodynamic heating. First row: vertical magnetic field evolution as simulated by the Advective Flux Transport model. Second row: potential magnetic field extrapolation of the AFT magnetograms. Third and fourth rows: integrated predicted radiance in Fe XVIII and 335 Å for a hydrodynamic state where each extrapolated loop is heated steadily (equation 1). This example corresponds to the magnetic flux evolution of NOAA 11726.

each coronal loop in the volume is then simulated with a 0D hydrodynamic model in an ad hoc steady heating approximation. While steady heating may be difficult to reconcile with the evolution of loops observed at $\lesssim 2 \times 10^6$ K (but see Mikić et al. 2013), it can help us understand the role that the magnitudes used in the parametrization of the heating play in the overall energy budget.

4.1. Magnetic flux decay

We model the magnetic flux decay of the active regions in our dataset using the AFT model, a surface flux trans-

port (SFT) model. SFT models simulate the displacement of the magnetic flux on the surface through the following flows: differential rotation, meridional circulation, and the cellular and turbulent motions of convection. AFT is distinct from other SFT models in the way it treats the transport of convective motions. Most models parametrize that transport as a diffusive process. AFT models it explicitly using a convective velocity field with the spectral characteristics of the flows observed on the Sun (Hathaway et al. 2010). A detailed description of the model can be found in Upton & Hathaway

(2014b,a). Paper I describes its application to our current active region dataset.

The baseline of the model assimilates magnetic flux density measurements from line-of-sight magnetograms, only available on the Earth side view of the Sun. The model evolves the flux everywhere else, where data is not available, until the region rotates back into view and the assimilation process resumes. To study the performance of the model for timescales longer than the fourteen day period that the active region rotates across the back of the Sun, assimilation can be turned off at any moment thus letting the flows govern the flux evolution for the remaining time of the experiment. In Paper I we used this option to forecast the decay of all active regions in the dataset from the moment they reached a peak in the total unsigned magnetic flux until full decay. In three of the regions (NOAA 11272, 11484, and 11726) that peak in flux happened while on the back side, so we used the 304 Å proxy to insert a bipolar region in the AFT maps and then allowed them to decay. The study showed that the AFT description provides realistic predictions of the decaying flux for periods longer than a solar rotation.

In the current study, we use the actual AFT magnetograms from those forecast calculations as the boundary conditions to model the magnetic field distribution in the corona. The AFT maps are Carrington projections of the full Sun at 0.35° resolution. We selected 9 – 11 AFT magnetograms per active region, encompassing the complete region’s lifetime from peak magnetic flux to the time when the 304 Å light curve had decayed to background levels. We deprojected the maps to heliographic coordinates at a spatial resolution of 1'' and extracted subareas of 512×512 pixels around the center of the active regions. The top row of Figure 3 shows a subset of the AFT simulated magnetograms for the NOAA 11726 fluxes. The simulated surface field distribution has many of the ingredients of an active region evolution besides a realistic flux decay: the polarities diffuse away and the surface flow pattern creates a reticulated field distribution characteristic of the active region plage.

4.2. Magnetic topology

Given the frozen-in conditions in the solar corona and assuming field aligned plasma flows, one way of modeling a full active region is by treating the hydrodynamics of each magnetic flux tube or loop independently. In this approximation, to identify the loops we need a description of how the magnetic field is distributed in the atmosphere. We use the minimum energy state, the potential field approximation — that is we extrapolate the field from the magnetograms into the corona using Fourier transform solutions to the Laplace’s equation for the scalar potential in a Cartesian coordinate system (e.g Nakagawa & Raadu 1972). This current free approximation is not necessarily the most accu-

rate description of the magnetic topology in an active region. Active regions are known to store magnetic energy in the form of currents, so present day state-of-the-art extrapolations are obtained in the non linear force free (NLFF) approximation (Wiegelmann & Sakurai 2012). We find, however, justified to use a simpler topological model in our study for two reasons. First, one of the interesting implications of the flux-luminosity relationship is that the radiative output correlates well with total unsigned magnetic flux, a quantity that is largely independent of the 3D topology. Fisher et al. (1998), for example, failed to find any correlation between X-ray luminosity and the non-potential components of the field inferred from vector data. Two active regions with the same magnetic flux, but different topologies and potentiality, should have approximately the same EUV emission, ignoring transient events. Second, we are not trying to reproduce the exact morphology and energetics in these regions. Instead, our goal is to find out whether a model that includes our basic understanding of flux transport, topology and heating is capable of reproducing observables in the active region decay. More complex descriptions will follow.

We used the AFT line-of-sight magnetograms as boundary conditions for the extrapolation and a field line tracing algorithm to identify field lines for every pixel (1'' resolution). We limited the search to magnetic flux densities in the range 20 – 900 Mx cm⁻² avoiding low signal-to-noise levels and the core of sunspots as they do not generally emit in the EUV. The panels in the second row of Figure 3 are examples of the magnetic topology model for NOAA 11726.

4.3. Coronal model

To simulate the total radiance of the active regions in the Fe XVIII and 335 Å passbands, we model the active regions as a set of independent loops. In these optically thin emission bands the loops’ intensities are fundamentally dependent on the plasma electron density and temperature at any given instant, with the total active region intensity simply the sum of all the loops. For every region we assign one loop per field line in the extrapolation and model their hydrodynamics using a 0D coronal model called “Enthalpy-based Thermal Evolution of Loops” EBTEL (Klimchuk et al. 2008; Cargill et al. 2012) that has been shown to provide results comparable to a state-of-the-art 1D model. We have used it in the past to study the envelope intensity lightcurve of a set of loops (Ugarte-Urra & Warren 2014). These coronal models, with their restricted field aligned dynamics, prevent us from addressing cross-field effects that can be important to understand the nature of the heating (e.g Dahlburg et al. 2016; Reale et al. 2016), but they allow us to do calculations that are not manageable today by 3D MHD codes.

EBTEL computes the evolution in time of spatially averaged properties of the loop such as coronal density and tem-

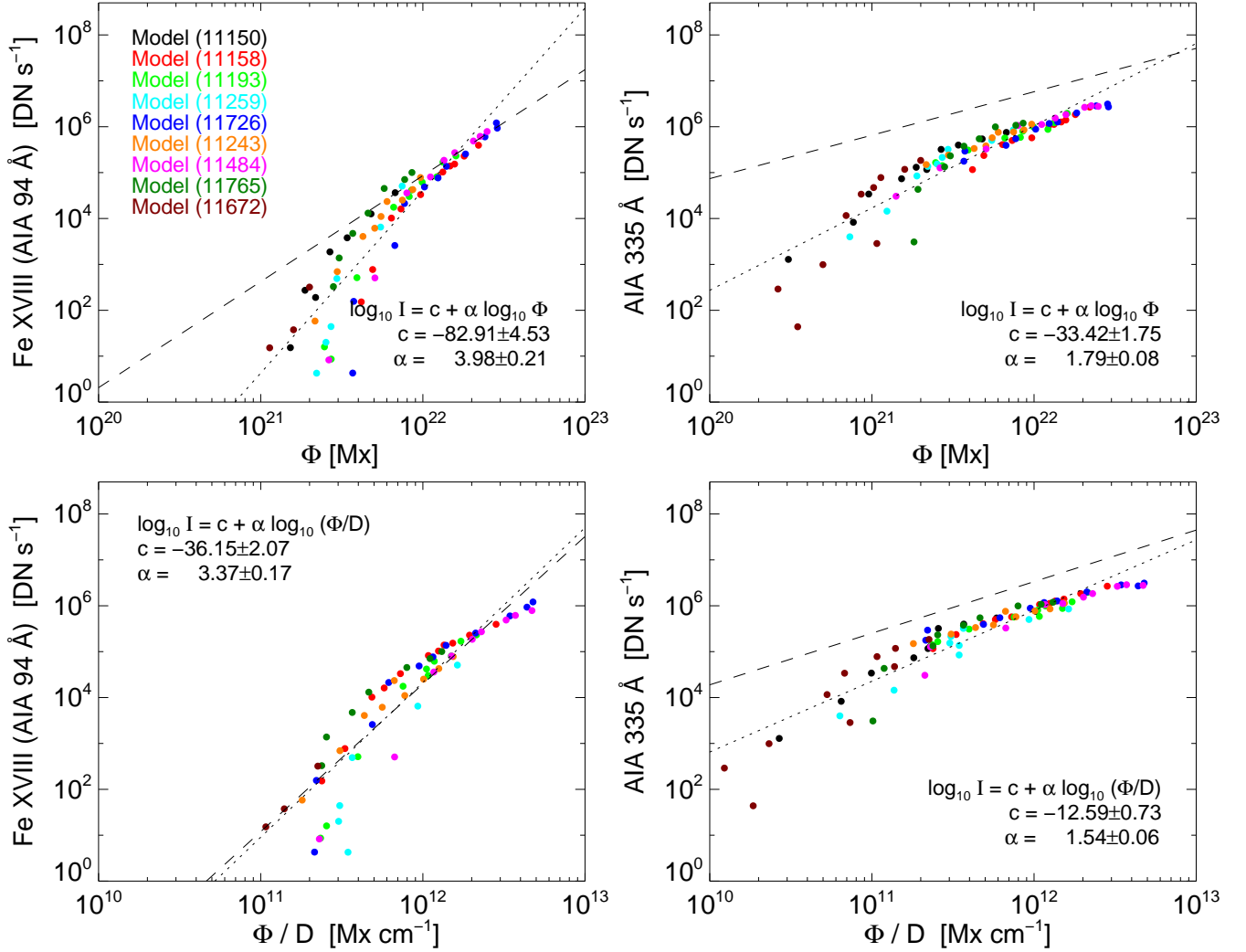


Figure 4. Scatterplot of the EUV radiance and total unsigned magnetic flux for the simulated active regions, not including any background intensities. Dotted lines are linear fits to simulation data. Dashed lines are the fits to the observational data in Figure 1.

perature in response to a variable heating. The only inputs are the loop’s length and the volumetric heating rate. The model was conceived to study the parameter space of impulsive heating events, but in the context of this study we have chosen to drop the time dependency and investigate a steady heating scenario with a volumetric heating rate of the form

$$\epsilon_H = \epsilon_0 \frac{\bar{B}}{B_0} \frac{L_0}{L} \quad (1)$$

where L is the total length of the loop and \bar{B} is the average field strength. Warren & Winebarger (2006) found that this functional form for the heating produces emission at high temperatures that is consistent with observations. In that study they choose ϵ_0 so that the loop $\bar{B} = \bar{B}_0 = 76$ G and $L = L_0 = 29$ Mm has an apex temperature of 4 MK and use a filling factor to match the intensities. Here we choose the same values for L_0 and \bar{B}_0 but leave ϵ_0 as a free vari-

able to match the observed intensities. In the context of other loop studies, the heating is coronal, steady and uniformly distributed and leads to a time independent equilibrium that balances heating with radiative losses.

For each loop, we compute the Fe XVIII and 335 Å counts using the AIA instrument response functions as a function of temperature, the coronal temperature and density returned by EBTEL given the \bar{B}/L heating rate, and the loop’s volume. We do not include the differential emission measure from the transition region. To estimate the AIA Fe XVIII response with no cool contribution, we compute the emissivity of the spectral line as a function of temperature with CHIANTI and scale it down to match the high temperature peak in the 94 Å response. We assume all loops to be cylinders of radius 350 km and length L determined by the extrapolation. The radius choice is convenient given the 1'' (725 km) resolution of the magnetograms and the extrapolation of one field line per

pixel. The assumption is also justified based on a recent studies of loop size measurements that argue that many observed loops are single monolithic structures at the scales of hundred of kilometers and are resolved by current instrumentation (Brooks et al. 2012, 2013; Aschwanden & Peter 2017). A constant loop width assumption is consistent with observations (Klimchuk 2000; López Fuentes et al. 2006), but still unexplained by magnetic field models. In the approximately force-free corona, these models predict a flux tube expansion with height result of the magnetic field strength falloff.

The total counts for each loop is then distributed along the corresponding $1''$ pixels of the extrapolation volume and projected to the plane of the image taking into account the area factor conversion from the default $0.6''$ per pixel in the AIA response. To mimic the optical response of the AIA instrument to a 350 km radius source, the projected images are convolved with a Gaussian filter with a full width half maximum (FWHM) of 1.47 pixels (1056 km), the apparent size for such a source in an instrument with FWHM point spread function of $1.14''$, that of AIA (Grigis et al. 2012). As a final step, we add noise to the images. For the 335 Å filter images we apply a poissonian photon distribution to the uncertainty estimates that can be obtained from the standard AIA software distribution (`aia_bp_estimate_error.pro`) in photons. In the case of Fe XVIII, there are no estimates because our images are a processed version of the 94 Å filter images, and we use an empirical relationship where the uncertainties scale as $(\text{DN s}^{-1})^{1/3}$, obtained in Ugarte-Urra & Warren (2014) from the standard deviation of sets of five consecutive 12s cadence images. Examples of simulated images can be seen in Figure 3 for NOAA 11726. While the magnetic flux decay is similar to that of the observed region, the magnetic topology and the simulated morphology in the EUV are not expected to match the observations.

Figure 4 presents the model results based on all assumptions above. The panels show the integrated counts per second as a function of total magnetic flux and flux divided by polarities separation for both Fe XVIII and 335 Å for all regions. As with the observations, we only considered pixels with radiance values above 2 DN s^{-1} (Fe XVIII) and 4 DN s^{-1} (335 Å), and magnetic flux densities within 90 – 900 G. The dashed lines in Figure 4 are the linear fits to the AIA and HMI data from Figure 1 for reference. To find this match, we only varied ϵ_0 . The adopted value is $0.005 \text{ ergs cm}^{-3} \text{ s}^{-1}$ which brings the Fe XVIII at high counts in close agreement to the measurements. Increasing ϵ_0 to 0.010 results in an order of magnitude increase for the Fe XVIII radiance and just about a factor of 2 for 335 Å, supporting our earlier argument that the Fe XVIII line is a better heating diagnostic. Given the simplicity of the assumptions, it seems remarkable how close the simulated flux - radiance pairs are to the actual measurements in terms of absolute numbers and trends

(slopes). Recall that the only data constraints to the model are the peak magnetic flux obtained from the 304 Å proxy that starts the AFT model forecast and the choice of ϵ_0 in the heating to match the Fe XVIII radiance levels. There are, nevertheless, obvious discrepancies that suggest that the model is still far from being a complete satisfactory description of the observations. We discuss below those discrepancies and potential improvements.

4.4. Discussion

We have shown in the previous section that the model is able to explain the order of magnitude change in both radiance and magnetic flux in the evolution of active regions. This is consistent with the results from Warren & Winebarger (2006) that used hydrostatic solutions with a \bar{B}/L scaling to reproduce the X-ray – flux relationship using real magnetograms. Our model with simulated magnetograms is able to reproduce the Fe XVIII slope for Φ/D , and for Φ at high radiance values, but a non-linear trend towards low fluxes seems apparent for both. This is also noticeable in 335 Å. In Fe XVIII, as the region decays and disappears, radiance reaches the few hundred DN s^{-1} level from the added contribution of several pixels close to the threshold level, so we may be reaching the limit of what can be diagnosed with a line like Fe XVIII and an AIA instrument response. While in Paper I we showed that the AFT model is able to predict the total flux of select active regions to within a factor of 2, there have not been detailed statistical comparisons between the AFT simulated active region evolution and observations. Potential discrepancies between the magnetic field distribution in AFT and real magnetograms could propagate into the heating scaling and need to be investigated.

The main discrepancies for the 335 Å scatterplot are total counts, with a systematic underestimation in the model, and a drop of radiance at small fluxes. The drop at small fluxes can be explained if we consider a background intensity. The model does not include loops that are not completely closed within the cartesian extrapolation domain and therefore ignores distant connectivities that can contribute with signal along the line-of-sight. The quiet Sun high altitude corona in which active regions are embedded is known from off-limb observations (e.g Warren & Brooks 2009) to emit at the $1-2 \times 10^6 \text{ K}$ temperature range. Similarly we expect an excess 335 Å intensity from small low lying loops that are not part of the extrapolation for their small footpoint field strength, but contribute to the line-of-sight observed intensity. One simple way of estimating these contributions is to look outside active regions. In those areas 335 Å images have intensities in the range $1.5 - 5 \text{ DN s}^{-1}$. Figure 5 shows a rendition of the model where a fixed background of 1.5 DN s^{-1} (335 Å) has been added to every pixel before noise. This is sufficient to prevent the drop of intensity at low fluxes where the back-

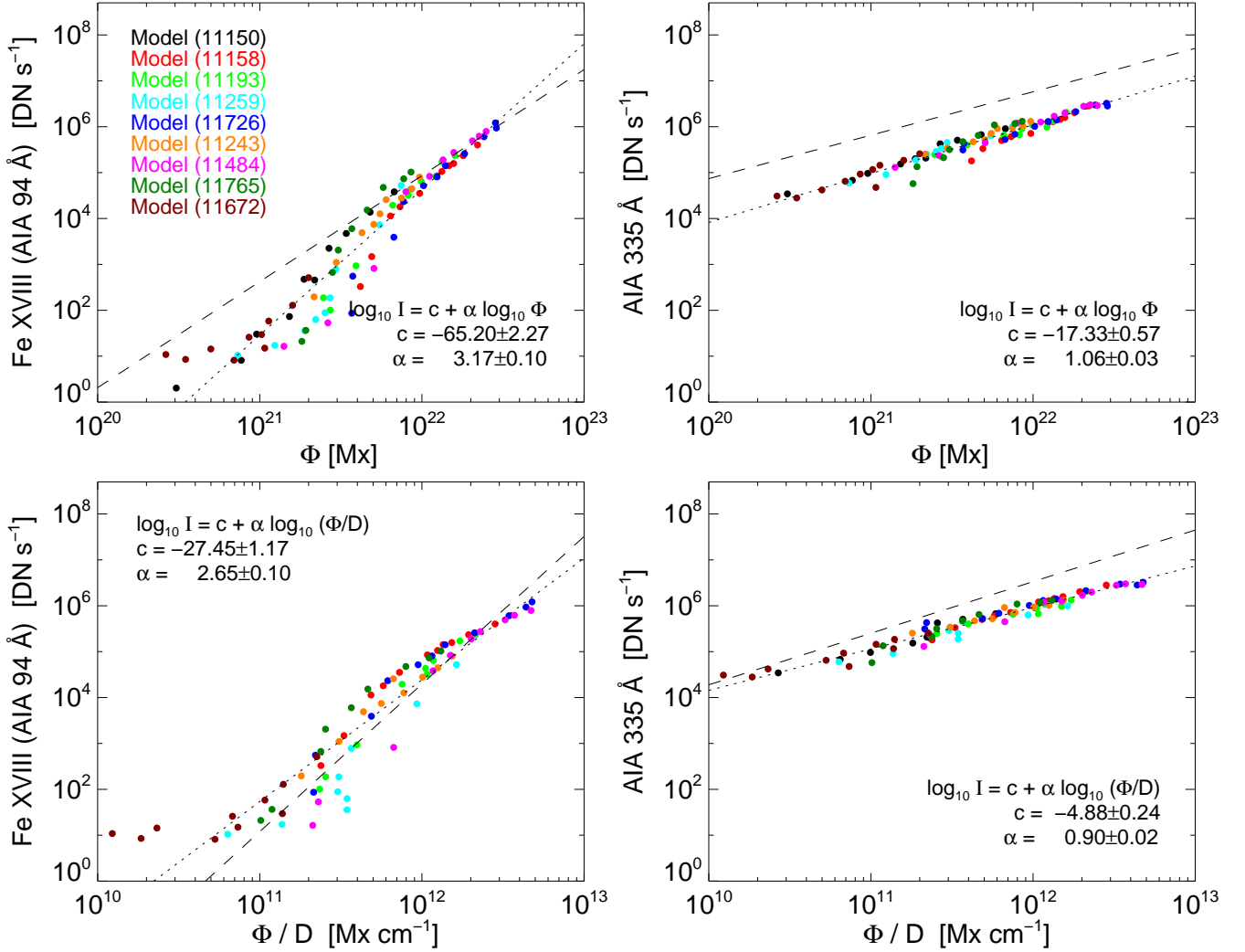


Figure 5. Scatterplot of the EUV radiance and total unsigned magnetic flux for the simulated active regions, including a background intensity of 0.1 and 1.5 DN s⁻¹ for Fe XVIII and 335 Å respectively. Dotted lines are linear fits to simulation data. Dashed lines are the fits to the observational data in Figure 1.

ground has a larger relative impact in each pixel, but it has no significant effect in the integration at high counts. The background outside active regions in Fe XVIII images is at the noise level, under 1 DN s⁻¹. While negligible, in Figure 5 we show the effect of a 0.1 DN s⁻¹ Fe XVIII background to maintain the symmetry in the analysis for both filters. It is evident that at low magnetic fluxes, corresponding to weaker fields, larger polarity separation and therefore smaller heating as prescribed, the background contribution can even dominate. Note that for the smallest magnetic fluxes, as the region decays, the Fe XVIII counts are dominated by contribution from the wings in the noise distribution leaking above the threshold. Indeed, the addition of the background accentuates this effect and raises the counts further introducing new data points in Figure 5 for the final time steps (lower fluxes) of regions 11150, 11259, 11484, 11672, 11765. Originally

those images had count levels under the threshold and therefore were not included in Figure 4.

Assuming that there are no calibration issues that could affect the relative intensities of Fe XVIII and 335 Å, the systematic underestimation of 335 Å intensity, a factor of 3 and 5 in Φ/D and Φ , is difficult to reconcile with the current model. Intensities are mainly dependent on density and temperature. In the current set up, to raise the 335 Å signal up to the observed values, we can either increase the density of existing loops, bringing the loop temperatures closer to the 335 Å filter response and away from Fe XVIII, or increase the volume of emission, i.e. the number of loops. Increasing the energy in the steady heating case has the effect of increasing simultaneously the density and temperature of the steady state. At the temperatures of 2 – 4 × 10⁶ K that the loops are already tuned to, this results in higher Fe XVIII intensities and a com-

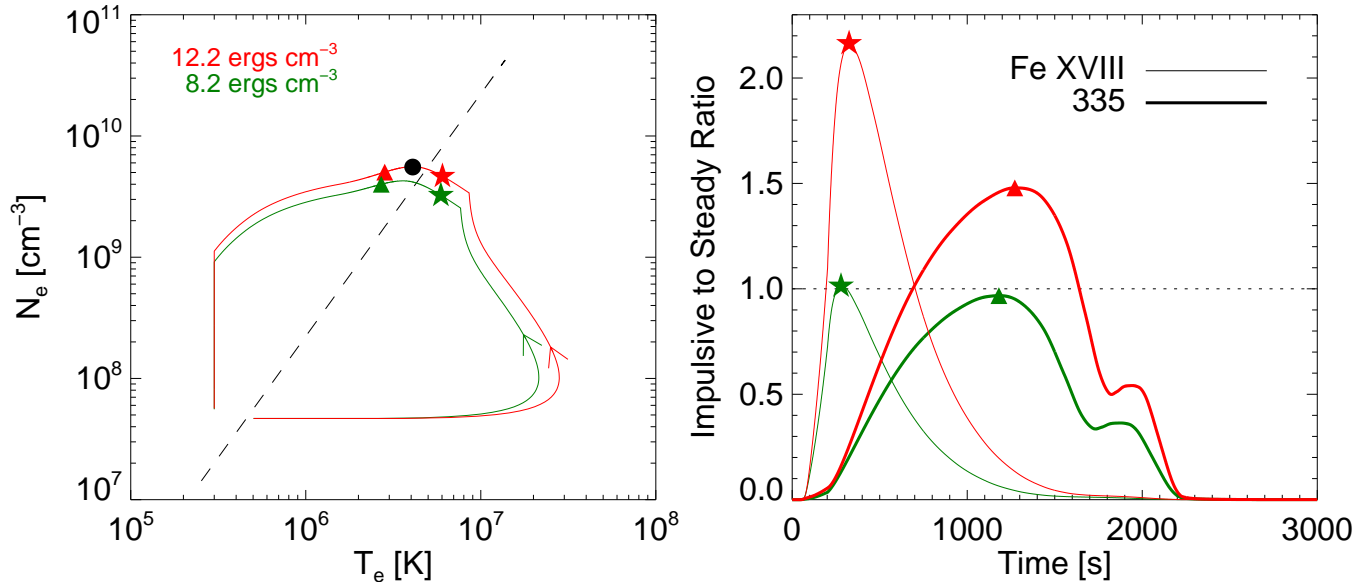


Figure 6. EBTEL simulations of a 59 Mm loop heated impulsively. The different colors represent two different volumetric heating energies. The left panel shows the density and temperature evolution, where the dashed line illustrates the hydrostatic solutions and the filled circle is the steady heating in our model. Arrows indicate direction of evolution. The right panel shows the ratio of the synthetic lightcurves for Fe XVIII and 335 Å with respect to the steady case (dotted line). The star and triangle symbols are references across the panels.

peting effect in 335 Å between the higher number of photons from the density enhancement and the smaller response of the filter at the growing temperature. The reverse, decreasing the energy, produces smaller than predicted Fe XVIII intensities. Increasing the number of steady loops, by means of filling more coronal volume with them, would in principle work in favor of increasing 335 Å signal because the space to fill grows with height and longer loops are cooler due to the L^{-1} dependence of the heating. It seems unlikely given that we are missing 2/3 of the signal and the longer loops are dimmer, but we can not completely rule out that steady heating could work if we were significantly underestimating the emitting volume.

There is, however, a more attractive explanation of the discrepancy and that is the choice of the heating model. Our choice of steady heating is based in simplicity and its past success in reproducing particular features of full active region modeling. Decades of studies of loop dynamics have, nevertheless, given us confidence that impulsive heating is likely to play a fundamental role in the evolution of the EUV loops observed at $\lesssim 2 \times 10^6$ K (see review and references in Reale 2014). Steady footpoint heating has also been proposed to describe these observations (see recent discussion Mikić et al. 2013; Klimchuk et al. 2010). The nature of the heating is ultimately likely to be impulsive and any effective steadiness is just a consequence of the frequency of recurrence of those events (e.g. Klimchuk 2006), with a probable scenario where various degrees of steadiness coexist and an intermediate case (heating frequency of the order of the cool-

ing time) dominates (Cargill et al. 2015). It is beyond the reach of this paper to implement impulsive heating, a significantly larger parameter space. We plan to do it in a forthcoming paper. We can show, however, that the effect of the impulsiveness would in fact be to move the intensities in the direction for a better match.

Figure 6 shows the EBTEL calculations for a 59 Mm loop taken from one of the initial snapshots in NOAA 11726. The filled circle represents the density and temperature solution in the steady case, as simulated throughout this paper. That density-temperature pair falls very close to the density and temperature solutions (dashed line) of hydrostatic equilibrium (Rosner et al. 1978). In the impulsive case, density and temperature change as a function of time (red and green lines for two energy values) and as pointed out by Winebarger & Warren (2004) the loop remains underdense before reaching its equilibrium point, at $\sim 4 \times 10^6$ K in this case. At that temperature and density, when the radiative losses begin to dominate, it is when the loop will radiate more in 335 Å, that is ~ 700 s into the time evolution of the red curve in Figure 6. The loop reaches the formation temperature of Fe XVIII (7×10^6 K) earlier, within the underdense section of the evolution. Therefore, one could in principle conclude that with an impulsive heating model, the loop will be underdense when emitting Fe XVIII and the adjustment in energy needed to match these new set of intensities would decrease the relative difference to 335 Å. This turns out to be true, but the explanation is not just in the density of the loop at the different stages. In the right panel of Figure 6

we show the ratio of Fe XVIII and 335 Å intensities to the steady case. If we fix the energy to match the peak Fe XVIII with the steady case (green curves) we see that both filters produce a ratio of 1 at peak, apparently disproving the differential effect. In the impulsive case, it is the combined effect of density and temperature sensitivity of the filter, where a differential factor is introduced, a factor of 2 in this particular example. The loops radiate longer in 335 Å. It is the time integrated intensity that raises the 335 Å emission with respect to Fe XVIII. In other words, with impulsive heating at any given time and line-of-sight we would expect to see more 335 Å loops, a result that works in the direction of reconciling the discrepancy that we find in the steady case. This needs to be demonstrated in a full, time-dependent active region simulation. The exercise in any case shows that Fe XVIII and Fe XVI are diagnostics of different phases in the loop evolution.

5. CONCLUSIONS

We present new measurements of the magnetic flux - EUV radiance relationship of solar active regions from observations of the AIA and HMI instruments on the SDO mission in the 335 Å passband and the Fe XVIII component of the 94 Å band. Nine active regions were observed over several stages of their evolution from birth to decay. We confirm past reports that a power law ($I \propto \Phi^\alpha$) is a good representation of the correlation and extend them to the Fe XVIII spectral line, a particularly good diagnostic for coronal heating in active regions, as it forms at a temperature very close to the characteristic peak of the emission measure distribution. We find, in fact, that a better indicator of the Fe XVIII radiance is the ratio of the total unsigned magnetic flux to the polarities separation (Φ/D) with a slope of $\alpha = 3.22 \pm 0.03$.

We then use these results to test our current understanding of active region magnetic field evolution and coronal heating. We use magnetograms, from simulations of the magnetic flux decay of these nine active regions produced by the Advective Flux Transport model in [Paper I](#), as a boundary condition for the potential magnetic topology in the coronal atmosphere. We then model the hydrodynamics of each field line independently with the EBTEL 0D model assuming steady heating that scales as \bar{B}/L . Finally, we integrate all loops to calculate the active regions' emission in Fe XVIII and 335 Å

and compare them to the magnetic fluxes and polarities separation from the AFT simulated magnetograms. We find that steady heating is able to partially reproduce slopes of the flux - radiance relationship for both lines, but find discrepancies on the magnitudes that we speculate could be resolved with impulsive heating, although this needs to be demonstrated in the future.

These results support the idea that our understanding of fundamental processes in the Sun such as the transport of magnetic fields on the solar surface, the distribution of magnetic fields in the corona and the plasma hydrodynamics along the loops have reached a level of maturity that allows us to couple them and do detailed quantitative comparisons to available data. There is significant progress to be made in all three aspects of the model, particularly in the topology and heating parts of our experiment that can already be upgraded with available tools such as NLFF and time dependent heating. This will be part of our future active region studies. Ultimately, we expect that 3D MHD models based on first principles will reach a point where they can address the spatial and temporal scales necessary to be tested in a similar manner as our quasi-static steady heating set up. Spectroscopy of high temperature lines such as Fe XVIII is a promising diagnostic of heating to confront to those models.

We would like to thank the anonymous referee for all the comments and suggestions that helped improve the paper. AIA and HMI data are courtesy of NASA/SDO and the AIA and HMI science teams. I.U.U. was supported by NASA Heliophysics Guest Investigator program. L.A.U. was supported by the NASA Heliophysics Guest Investigator program and by the National Science Foundation Atmospheric and Geospace Sciences Postdoctoral Research Fellowship Program. The National Center for Atmospheric Research is sponsored by the National Science Foundation. P.R.Y. was supported by NASA grant NNX13AE06G.

Facilities: SDO (AIA,HMI)

Software: CHIANTI ([Dere et al. 1997](#)), SolarSoft ([Freeland & Handy 2012](#))

REFERENCES

- Aschwanden, M. J., & Peter, H. 2017, ArXiv e-prints
- Benevolenskaya, E. E., Kosovichev, A. G., Lemen, J. R., Scherrer, P. H., & Slater, G. L. 2002, *ApJL*, 571, L181
- Bingert, S., & Peter, H. 2011, *A&A*, 530, A112
- Bourdin, P.-A., Bingert, S., & Peter, H. 2013, *A&A*, 555, A123
- Brooks, D. H., Warren, H. P., & Ugarte-Urra, I. 2012, *ApJL*, 755, L33
- Brooks, D. H., Warren, H. P., Ugarte-Urra, I., & Winebarger, A. R. 2013, *ApJL*, 772, L19
- Cargill, P. J., Bradshaw, S. J., & Klimchuk, J. A. 2012, *ApJ*, 752, 161

- Cargill, P. J., Warren, H. P., & Bradshaw, S. J. 2015, *Philosophical Transactions of the Royal Society of London Series A*, 373, 20140260
- Dahlburg, R. B., Einaudi, G., Taylor, B. D., Ugarte-Urra, I., Warren, H. P., Rappazzo, A. F., & Velli, M. 2016, *ApJ*, 817, 47
- Dere, K. P., Landi, E., Mason, H. E., Monsignori Fossi, B. C., & Young, P. R. 1997, *A&AS*, 125
- Dudík, J., Dzifčáková, E., Karlický, M., & Kulinová, A. 2011, *A&A*, 531, A115
- Fisher, G. H., Longcope, D. W., Metcalf, T. R., & Pevtsov, A. A. 1998, *ApJ*, 508, 885
- Fludra, A., & Ireland, J. 2003, *A&A*, 398, 297
—, 2008, *A&A*, 483, 609
- Fludra, A., Ireland, J., Del Zanna, G., & Thompson, W. T. 2002, *Advances in Space Research*, 29, 361
- Freeland, S. L., & Handy, B. N. 2012, *SolarSoft: Programming and data analysis environment for solar physics*, *Astrophysics Source Code Library*, record ascl:1208.013
- Grigis, P., Su, Y., & Weber, M. 2012, AIA Team Online Document, <http://hesperia.gsfc.nasa.gov/ssw/sdo/aia/idl/psf/DOC/psfreport.pdf>
- Gudiksen, B. V., & Nordlund, Å. 2005, *ApJ*, 618, 1020
- Gurman, J. B., Withbroe, G. L., & Harvey, J. W. 1974, *SoPh*, 34, 105
- Hansteen, V. H., Hara, H., De Pontieu, B., & Carlsson, M. 2010, *ApJ*, 718, 1070
- Hathaway, D. H., Williams, P. E., Dela Rosa, K., & Cuntz, M. 2010, *ApJ*, 725, 1082
- Klimchuk, J. A. 2000, *SoPh*, 193, 53
—, 2006, *SoPh*, 234, 41
- Klimchuk, J. A., Karpen, J. T., & Antiochos, S. K. 2010, *ApJ*, 714, 1239
- Klimchuk, J. A., Patsourakos, S., & Cargill, P. J. 2008, *ApJ*, 682, 1351
- Lemen, J. R., et al. 2012, *SoPh*, 275, 17
- López Fuentes, M. C., Klimchuk, J. A., & Démoulin, P. 2006, *ApJ*, 639, 459
- Lundquist, L. L., Fisher, G. H., & McTiernan, J. M. 2008a, *ApJS*, 179, 509
- Lundquist, L. L., Fisher, G. H., Metcalf, T. R., Leka, K. D., & McTiernan, J. M. 2008b, *ApJ*, 689, 1388
- Mandrini, C. H., Démoulin, P., & Klimchuk, J. A. 2000, *ApJ*, 530, 999
- Martínez-Sykora, J., De Pontieu, B., Testa, P., & Hansteen, V. 2011, *ApJ*, 743, 23
- Mikić, Z., Lionello, R., Mok, Y., Linker, J. A., & Winebarger, A. R. 2013, *ApJ*, 773, 94
- Mok, Y., Mikić, Z., Lionello, R., Downs, C., & Linker, J. A. 2016, *ApJ*, 817, 15
- Mok, Y., Mikić, Z., Lionello, R., & Linker, J. A. 2005, *ApJ*, 621, 1098
- Nakagawa, Y., & Raadu, M. A. 1972, *SoPh*, 25, 127
- O'Dwyer, B., Del Zanna, G., Mason, H. E., Weber, M. A., & Tripathi, D. 2010, *A&A*, 521, A21
- Olluri, K., Gudiksen, B. V., Hansteen, V. H., & De Pontieu, B. 2015, *ApJ*, 802, 5
- Pesnell, W. D., Thompson, B. J., & Chamberlin, P. C. 2012, *SoPh*, 275, 3
- Peter, H., Gudiksen, B. V., & Nordlund, Å. 2004, *ApJL*, 617, L85
—, 2006, *ApJ*, 638, 1086
- Pevtsov, A. A., Fisher, G. H., Acton, L. W., Longcope, D. W., Johns-Krull, C. M., Kankelborg, C. C., & Metcalf, T. R. 2003, *ApJ*, 598, 1387
- Reale, F. 2014, *Living Reviews in Solar Physics*, 11, 4
- Reale, F., Orlando, S., Guarrasi, M., Mignone, A., Peres, G., Hood, A. W., & Priest, E. R. 2016, *ApJ*, 830, 21
- Rosner, R., Tucker, W. H., & Vaiana, G. S. 1978, *ApJ*, 220, 643
- Scherrer, P. H., et al. 2012, *SoPh*, 275, 207
- Schou, J., et al. 2012, *SoPh*, 275, 229
- Schrijver, C. J. 1987, *A&A*, 180, 241
- Schrijver, C. J., Sandman, A. W., Aschwanden, M. J., & De Rosa, M. L. 2004, *ApJ*, 615, 512
- Teriaca, L., Warren, H. P., & Curdt, W. 2012, *ApJL*, 754, L40
- Testa, P., De Pontieu, B., Martínez-Sykora, J., Hansteen, V., & Carlsson, M. 2012, *ApJ*, 758, 54
- Testa, P., & Reale, F. 2012, *ApJL*, 750, L10
- Ugarte-Urra, I. 2004, PhD thesis, Queen's University of Belfast (United Kingdom), Northern Ireland
- Ugarte-Urra, I., Upton, L., Warren, H. P., & Hathaway, D. H. 2015, *ApJ*, 815, 90
- Ugarte-Urra, I., & Warren, H. P. 2012, *ApJ*, 761, 21
—, 2014, *ApJ*, 783, 12
- Upton, L., & Hathaway, D. H. 2014a, *ApJ*, 792, 142
—, 2014b, *ApJ*, 780, 5
- van Driel-Gesztelyi, L., Démoulin, P., Mandrini, C. H., Harra, L., & Klimchuk, J. A. 2003, *ApJ*, 586, 579
- van Driel-Gesztelyi, L., & Green, L. M. 2015, *Living Reviews in Solar Physics*, 12, 1
- Warren, H. P., & Brooks, D. H. 2009, *ApJ*, 700, 762
- Warren, H. P., & Winebarger, A. R. 2006, *ApJ*, 645, 711
—, 2007, *ApJ*, 666, 1245
- Warren, H. P., Winebarger, A. R., & Brooks, D. H. 2012, *ApJ*, 759, 141
- Wiegmann, T., & Sakurai, T. 2012, *Living Reviews in Solar Physics*, 9, 5
- Winebarger, A. R., & Warren, H. P. 2004, *ApJL*, 610, L129
- Winebarger, A. R., Warren, H. P., & Falconer, D. A. 2008, *ApJ*, 676, 672
- Zacharias, P., Bingert, S., & Peter, H. 2009, *Advances in Space Research*, 43, 1451
- Zacharias, P., Peter, H., & Bingert, S. 2011, *A&A*, 531, A97